

Flexible Bifunctional Electrode for Alkaline Water Splitting with Long-Term Stability

Abhijit Ganguly, Ruairi J. McGlynn, Adam Boies, Paul Maguire, Davide Mariotti, and Supriya Chakrabarti*



Cite This: *ACS Appl. Mater. Interfaces* 2024, 16, 12339–12352



Read Online

ACCESS |



Metrics & More



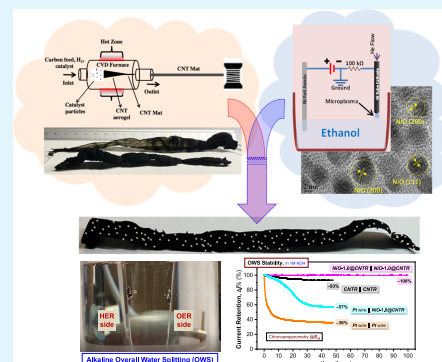
Article Recommendations



Supporting Information

ABSTRACT: Progress in electrochemical water-splitting devices as future renewable and clean energy systems requires the development of electrodes composed of efficient and earth-abundant bifunctional electrocatalysts. This study reveals a novel flexible and bifunctional electrode ($NiO@CNTR$) by hybridizing macroscopically assembled carbon nanotube ribbons ($CNTRs$) and atmospheric plasma-synthesized NiO quantum dots (QDs) with varied loadings to demonstrate bifunctional electrocatalytic activity for stable and efficient overall water-splitting (OWS) applications. Comparative studies on the effect of different electrolytes, e.g., acid and alkaline, reveal a strong preference for alkaline electrolytes for the developed $NiO@CNTR$ electrode, suggesting its bifunctionality for both HER and OER activities. Our proposed $NiO@CNTR$ electrode demonstrates significantly enhanced overall catalytic performance in a two-electrode alkaline electrolyzer cell configuration by assembling the same electrode materials as both the anode and the cathode, with a remarkable long-standing stability retaining $\sim 100\%$ of the initial current after a 100 h long OWS run, which is attributed to the “synergistic coupling” between NiO QD catalysts and the CNTR matrix. Interestingly, the developed electrode exhibits a cell potential (E_{10}) of only 1.81 V with significantly low NiO QD loading ($83 \mu\text{g}/\text{cm}^2$) compared to other catalyst loading values reported in the literature. This study demonstrates a potential class of carbon-based electrodes with single-metal-based bifunctional catalysts that opens up a cost-effective and large-scale pathway for further development of catalysts and their loading engineering suitable for alkaline-based OWS applications and green hydrogen generation.

KEYWORDS: bifunctional and flexible electrode, macroscopically assembled carbon nanotube (CNT) ribbons, nickel oxides (NiO) quantum dots (QDs), plasma-induced nonequilibrium electrochemistry (PiNE), hydrogen evolution reaction (HER), oxygen evolution reaction (OER), water electrolysis, overall water splitting (OWS) in alkaline media, alkaline electrolyzer cell, long-term OWS stability



1. INTRODUCTION

Alternative clean energy sources are essential to avoid the harmful impacts of fossil fuel^{1,2} to produce a cleaner environment. In this regard, electrochemical water electrolysis is a promising sustainable technology for the large-scale production of hydrogen as a clean fuel.^{3–6} Industrial-scale application of water electrolyzer cells is difficult without replacing the expensive platinum-based electrode for hydrogen evolution reaction (HER) and electrodes based on Ir/Ru for oxygen evolution reaction (OER).⁷ It is necessary to develop alternative earth-abundant, low-cost, stable, and efficient electrodes made of non-noble metal compounds.^{4–8} Likewise, the development of a bifunctional electrocatalyst is becoming increasingly important to achieve a significant leap in this technology to avoid the complexity of using different electrodes for HER and OER in the electrolyzer cell.^{4–6,8–16} Generally different electrodes for HER and OER show electrolyte preferences for their best performance, e.g., Ir/Ru-based OER catalysts prefer an alkaline solution, while Pt-based HER catalysts exhibit high

activities in acidic electrolytes.^{6–8,14,17} In addition to the high cost, Pt-based electrodes deteriorate due to their time-dependent drift¹⁸ and CO deactivation,¹⁹ which also justifies the development of an alternative bifunctional electrocatalyst with long-term operation stability throughout the lifetime of the single-electrolyte-based water electrolyzer cell.

In this work, we report the development of $NiO@CNTR$ hybrids with varied loadings of NiO QDs on the surface of CNTR as a potential class of a carbon-based bifunctional electrode with superior electrocatalytic activity and long-standing operation stability for overall water splitting (OWS) in alkaline electrolyzer cells. We have synthesized macroscopic

Received: August 31, 2023

Revised: January 25, 2024

Accepted: February 13, 2024

Published: March 1, 2024



Macroscopically assembled CNT ribbons, CNTR

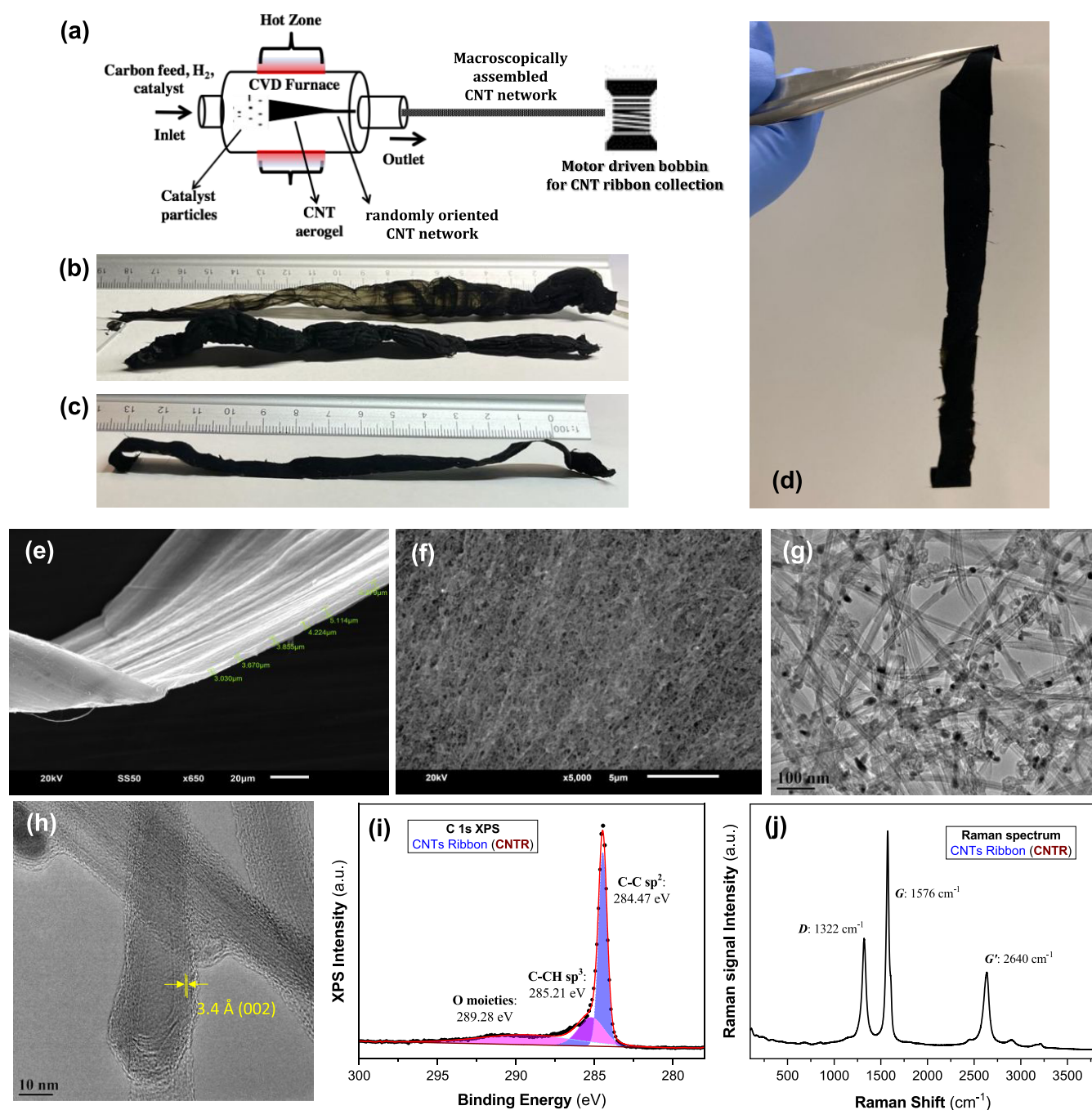


Figure 1. Macroscopically assembled CNT ribbon, CNTR. (a) Schematic diagram of the CVD system used for the winding of continuous CNT ribbons (CNTR). Representative images of (b) typical as-synthesized 3D ensemble of the randomly oriented CNT network and (c-d) flat and flexible CNTR after compression. (e) SEM image of a CNTR showing thickness in the range of 3–4 μm. (f) SEM image of the top surface of a CNTR at higher magnification showing dense packing and random orientation of the nanotubes. (g) TEM image and (h) high-resolution TEM image of the CNTR with an interlayer spacing of 3.4 Å, corresponding to the (002) plane. (i) High-resolution XPS spectrum of C 1s and (j) Raman spectrum of pristine CNTR.

assemblies of carbon nanotubes (CNTs) in the form of a ribbon (CNTR) directly spun from the chemical vapor deposition (CVD) reactor,^{20–23} which provides a competitive advantage over the conventional technique where CNTs are embedded in a host matrix and suffer from their poor dispersibility.^{24,25} Stable and quantum-confined NiO QDs in the form of colloids were synthesized by atmospheric plasma-induced nonequilibrium

electrochemistry (PiNE).²⁶ The NiO QD colloids were then spray-coated onto the CNTR surface to make NiO@CNTR electrodes. The proposed bifunctional electrode showed an excellent OWS catalytic performance (cell potential window, E_{10} , of 1.81 V), significantly better than a metallic Pt wire electrode (E_{10} of 2.15 V). The chronoamperometric study revealed that the NiO@CNTR electrode has long-term current

stability, close to 100% over 100 h of OWS run, much higher than the *Pt* wire electrode, which showed only a 36% current retention over 48 h.

We also demonstrated that the pristine electrode (CNTR, zero loading of NiO QDs) exhibited promising bifunctional electrocatalytic performances for alkaline-based OWS with an E_{10} of 2.11 V, better than that of the *Pt* wire electrode (\sim 2.15 V) and with significantly better stability (retaining \sim 94% of the initial current after a 48 h long run) than *Pt* (retaining only 36%), suggesting its potential application for a practical two-electrode OWS device in alkaline electrolyte. A comparative study of HER activity in acidic and alkaline media revealed that the CNTR and NiO@CNTR electrodes prefer alkaline media over acid.

The novelty of this work primarily lies with the proposed electrode materials composed of CNTR and PiNE-synthesized highly stable NiO QDs. The electrode support material CNTR is novel, which is the bulk form of network structured carbon nanotubes and holds superior properties such as chemical robustness, high electrical conductivity, and compatibility with various metal and metal oxide nanostructured catalysts. The synthesis process of CNTR is scalable with no length limitation, and its macroscopic form provides the flexibility to engineer these materials in terms of shape and size. Furthermore, the binder-free direct attachment of NiO QDs with CNTR provides a clear interface between the catalyst and the electrode support and shows excellent chemical and mechanical stability of NiO@CNTR hybrids, which is beneficial for achieving the observed “long-term” stability in OWS performance. Another novelty of this work is the successful application of the spray-coating technique for the desirable catalyst loading onto CNTR, which gives the advantage of the ease, rapidness, and scalability of the electrode fabrication. This study demonstrates the proposed NiO@CNTR electrode as a potential class of novel carbon-based electrodes and CNTR as an effective support for further catalyst development suitable for alkaline-based OWS applications and green hydrogen generation.

2. RESULTS AND DISCUSSION

2.1. Macroscopically Assembled CNT Ribbon, CNTR.

Macroscopically assembled CNT ribbons (CNTRs) were synthesized using a floating catalyst-assisted thermal CVD technique.^{20,22,23} This method can produce macroscopic assemblies of individual CNTs in a single step, where the CNTR can be directly drawn from the CVD furnace chamber without an obvious limit to the length of the material. Figure 1a shows the schematic diagram of the CVD system used for the winding of continuous CNTR from the chamber. In the “Section 4”, a detailed principle and procedure of the CNTR synthesis is illustrated, following our earlier publication by Brunet et al.²⁰

In the Supporting Information (SI, Section S2), Supporting Figure S1a,b demonstrates the direct dragging of the ribbon-like macroscopically assembled CNT network from the furnace chamber. Figure 1b represents a typical as-synthesized 3D ensemble of the randomly oriented CNT network (Figure S1c,d), which was further processed to form a flat and compact fabric-like material (shown in Figure 1c,d) prior to any characterization or application. Figure S1e–k reveals the flexible and lightweight nature of a typical CNTR (also see the Supporting Video SV1_CNTR). The detailed compaction process is mentioned in the Section 4 under “Section 4.2”. Depending on the pressure applied, the thickness of the final CNTR material can be controlled. In this study, the CNTR

thickness was maintained within 3–5 μ m. The material (CNTR) and its synthesis process were extensively characterized in our previous publication.²⁷

Figure 1e represents a scanning electron microscopy (SEM) image of a flat and compact CNTR sample. The representative thickness of the CNTR used in this report is between 3 and 5 μ m. The top-view SEM image of a CNTR (Figure 1f) shows dense packing and randomly entangled individual CNTs forming a ribbon composed of a three-dimensional (3D) macroscopic assembly. A representative transmission electron microscopy (TEM) image, shown in Figure 1g, depicts individual nanotubes with an average diameter of 20 nm. Typical high-resolution TEM (HRTEM) observation (Figure 1h) indicates that the CNTs are multiwalled nanotubes with an interlayer spacing of 3.4 Å, corresponding to the (002) plane. Further, HRTEM investigation (Figure S2a,b) and the electron energy loss spectroscopy (EELS) spectrum mapping images (Figure S2c) have also revealed the presence of Fe catalysts encapsulated inside the nanotubes.

X-ray photoelectron spectroscopic (XPS) analysis of the pristine CNTR was performed to understand the chemical composition of the CNTs. Deconvolution of the high-resolution XPS spectrum of the C 1s spectrum, shown in Figure 1i, resolved three distinct peaks centered at 284.47, 285.21, and 289.28 eV. The peak at 284.47 eV can be attributed to the aromatic carbon bonding (C–C sp^2)²⁸ from the hexagonal walls of the CNTs. The peak at 285.2 eV refers to the C–CH sp^3 bond, which is related to defects in the aromatic structure.²⁹ The broad peak centered at 289.28 eV appears due to the combined effect of different surface chemical bindings of HO–C=O or COOH, C–O, C=O, and O–C=O.²⁸

Raman spectroscopy has proven to be an effective and noninvasive tool to obtain experimental information about the electronic and vibrational properties of the CNTs.^{30,31} Figure 1j shows a typical Raman spectrum of pristine CNTR, which depicts three peaks at 1322, 1576, and 2640 cm^{-1} , corresponding to the D-band, the G-band, and the G'-band, respectively. Since the presence of defects in the CNT lattice enables elastic scattering processes, the area or intensity of the D-band scales with the concentration of defects within a CNT sample and can be used as an indicator of poor crystallinity.³² The G-band peak area or intensity is a measure of carbon nanotube graphitization and is related to the graphite tangential E_{2g} Raman active mode where the two carbon atoms in the graphene unit cell are vibrating tangentially one against the other. The G-band to D-band ratio indicates the graphitization to defect content ratio of the synthesized CNTs. Here, the G-band to D-band ratio (ratio of two peak areas) is found to be 2.29 ± 0.03 , representing a high degree of graphitization in the as-synthesized CNTR. This high degree of graphitization suggests high purity^{23,30} with large sp^2 domains²⁸ on the hexagonal walls of the nanotubes of the CNTR. This provides structural stability and extended electrocatalytic active sites,^{33,34} essential for high-performance catalytic electrodes.

2.2. NiO Quantum Dots (QDs) and NiO@CNTR Electrodes. NiO quantum dots (QDs) were synthesized using atmospheric plasma-induced nonequilibrium electrochemistry (PiNE).^{26,35–37} The digital image and the schematic diagram of the PiNE setup are shown in Figure S4a,b, respectively. Full details of the NiO QD synthesis procedure are illustrated in the Section 4 (under “Section 4.3”). As demonstrated in our earlier publication by Chakrabarti et al.,²⁶ the PiNE-synthesized NiO QDs possess a narrow size distribution with an average diameter

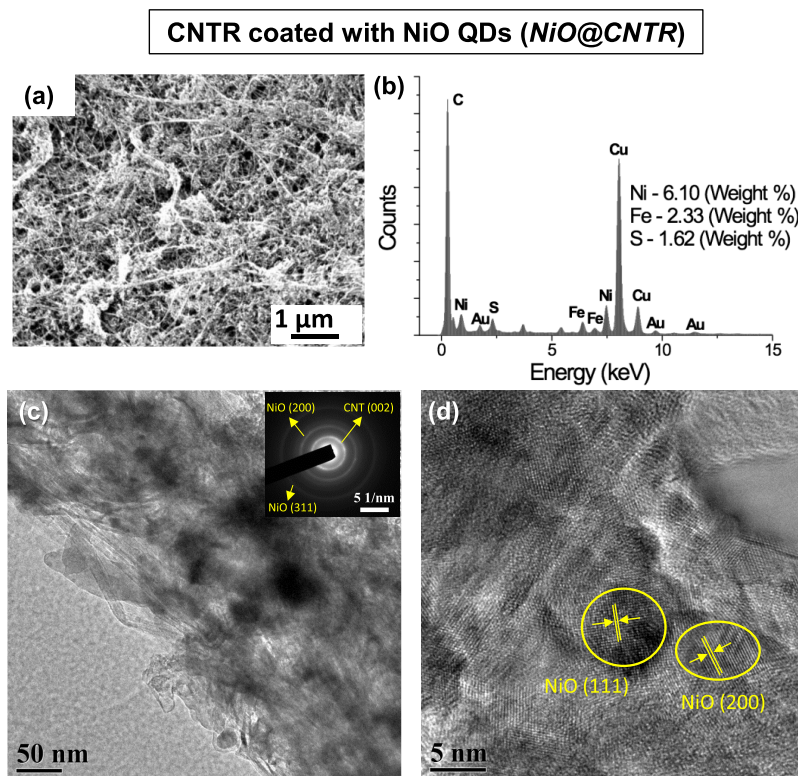


Figure 2. Nickel oxide (NiO) quantum dot (QD)-coated CNTR. (a) SEM image of a representative CNTR coated with NiO QD colloids (*NiO*-1.0). (b) EDX spectrum confirming the presence of NiO QDs on CNTR. Fe and S signals originate from the residual catalysts, and Cu originates from the TEM grid. (c) TEM micrograph of *NiO@CNTR*, and the inset shows the crystalline phase of the cubic NiO and (002) plane of CNTs. (d) Representative lattice-resolved HRTEM image of *NiO@CNTR* showing the high-resolution view of NiO particles on the CNTR matrix.

of 3 nm in the quantum confinement regime (Figure S4c). The lattice spacing measurements and the SAED pattern obtained from HRTEM images (Figure S4d,e) show clear lattice fringes corresponding to the (200) and (111) planes of the cubic NiO phase [JCPDS-No.: 47-1049]. Elemental characterization via XPS analysis clearly reveals the presence of the Ni $2p^{3/2}$ peak (Figure S4f). After deconvolution, three peaks can be extracted from the spectrum, which is in good agreement with previously reported NiO films synthesized by various techniques.^{26,38–40} The XPS peak centered at 853.5 eV indicates the presence of Ni²⁺ in the Ni–O octahedral bonding of cubic rocksalt NiO.^{39,40} The peak centered at 855.1 eV can be attributed to the vacancy-induced Ni³⁺ ion⁴¹ or nickel hydroxides and oxyhydroxides.⁴² Finally, the broad peak centered at 860.1 eV is due to the shakeup process³⁹ in the NiO structure.

For electrode preparation, the CNTR pieces were manually interlaced with adhesive copper tape and nickel conducting paste, enlarging the electrical contact for current collection. Subsequently, the whole assembly was laminated, maintaining a window (for the electrochemical reaction) of a 0.45 cm diameter, as shown in Figure S3a. Prior to the electrocatalytic measurements, the laminated CNTR electrodes were tested and optimized by employing conventional electrochemical characterizations (details are given in SI, Section S2 and Figure S3b–d). No leakage through lamination and wetting of the CNTR surface were observed, which confirms zero interference of the metal contact (adhesive Cu tape or Ni conducting paste) with the electrolyte solution.

For fabrication of NiO QD-coated CNTR electrodes (*NiO@CNTR*), the PiNE-synthesized NiO QD-ethanol colloids were spray-coated onto the laminated CNTR electrodes at three

different volume concentrations, 66 $\mu\text{g/mL}$ (as-synthesized colloids, symbolized as *NiO*-1.0), 33 $\mu\text{g/mL}$ (two times diluted, named as *NiO*-0.5), and 6.6 $\mu\text{g/mL}$ (diluted by ten times, symbolized as *NiO*-0.1). Here, it is crucial to confirm that, for the symbol used for the NiO QD colloids, the numeric value represents the dilution factor, not any chemical composition. Detailed spray-coating parameters and NiO QD loading concentration are given in the “Section 4” and Table S1 of the Supporting Information. In summary, the three different *NiO@CNTR* electrodes, namely *NiO*-1.0@CNTR, *NiO*-0.5@CNTR, and *NiO*-0.1@CNTR, were loaded by 83, 42, and 8.3 $\mu\text{g/cm}^2$ of NiO QDs, respectively. For comparison, the pristine CNT ribbon was also tested as an electrode (*CNTR*), representing its electrocatalytic activity without any additional catalyst. Notably, in this study, the maximum loading of NiO QDs as a catalyst ($\sim 83 \mu\text{g/cm}^2$ for the *NiO*-1.0@CNTR electrode) is 3–20 times lower than the average catalyst loading values reported in the literature.^{9,10,13,14,16,43–47} The NiO QD loading was optimized to achieve the minimum possible concentration for maximum performance, which will facilitate its applicability on an industrial scale, favoring the low-weight and low-cost approach.

The SEM image in Figure 2a shows NiO QDs coated on a CNTR, and the TEM-based EDS spectrum (Figure 2b) of *NiO@CNTR* reveals the presence of a Ni element in addition to carbon, confirming the presence of NiO QDs on the surface of CNTR. The TEM micrograph (Figure 2c) and the corresponding SAED pattern (inset, Figure 2c) of a *NiO@CNTR* sample indicate both the crystalline phase of cubic NiO and the (002) plane of CNT. The lattice-resolved HRTEM image shown in Figure 2d displays lattice fringes corresponding to the (200) and (111) planes of the cubic NiO phase [JCPDS-No.: 47-1049],

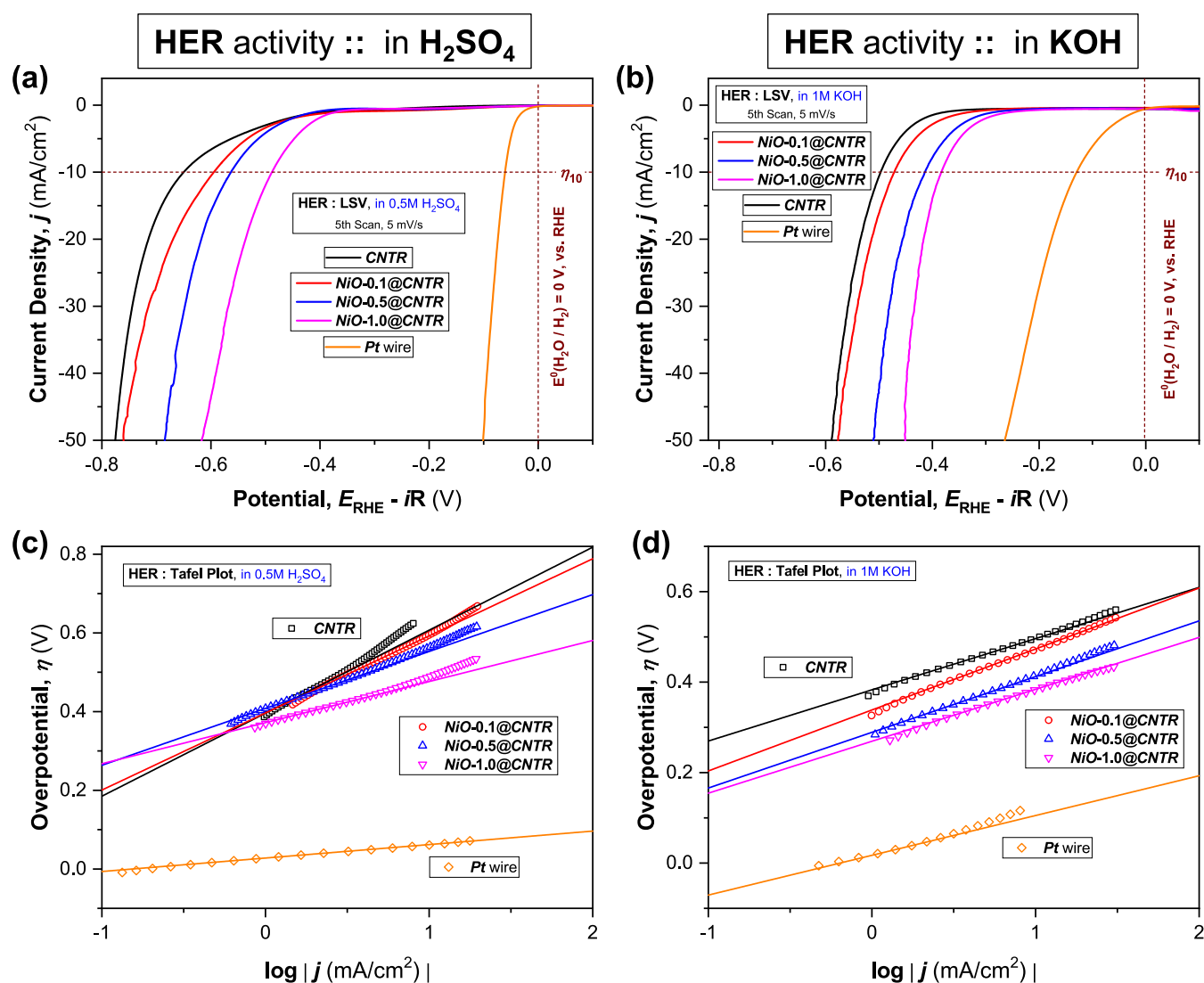


Figure 3. Electrocatalytic activity of pristine (*CNTR*) and NiO QD-coated (*NiO@CNTR*) electrodes. (a, b) Electrocatalytic activity for the hydrogen evolution reaction (HER) in N_2 -saturated aqueous (a) acidic (0.5 M H_2SO_4) and (b) alkaline (1 M KOH) media at a potential scan rate (ν) of 5 mV/s, without any rotation of the working electrode. (c, d) Corresponding Tafel plots of overpotential (η) vs $\log(j)$ measured in (c) 0.5 M H_2SO_4 and (d) 1 M KOH, where j represents the cathodic current density; all potentials were presented after iR correction. Respective data measured at the commercial *Pt* wire electrode are presented for comparison. Full details of the Tafel analysis and its associated calculations are described in the SI (Section S1, Analysis and Equations).

clearly indicating that the NiO QDs were successfully integrated on the *CNTR*. For the *NiO@CNTR* hybrid sample after spray-coating of a NiO colloidal solution on *CNTR*, the NiO particle size was found to be slightly larger (Figure 2c,d) in comparison to the as-synthesized NiO QDs (as displayed in Figure S4d) because of agglomeration between the neighboring QDs (imperfection in the manual process of spray-coating) and/or embedment of ultrasmall particles beneath the entangled CNTs, which make them difficult to image through TEM.

2.3. Electrocatalytic Activities of Pristine (*CNTR*) and NiO QD-Coated (*NiO@CNTR*) Electrodes. **2.3.1. Hydrogen Evolution Reaction (HER) Activity.** HER-catalytic performances of the laminated *CNTR* and *NiO@CNTR* electrodes were tested in N_2 -saturated acidic (0.5 M H_2SO_4 , Figure 3a) and alkaline electrolytes (1 M KOH, Figure 3b). For comparison, the HER activities of a commercial *Pt* wire electrode were measured and are presented in Figure 3.

Three important observations follow from the iR -corrected polarization curves (linear sweep voltammograms, LSV plots, Figure 3a,3b):

- (1) The pristine CNT ribbon electrode (*CNTR*, zero loading of NiO QDs) exhibited reasonable HER performances in both acidic (0.5 M H_2SO_4 , Figure 3a) and alkaline (1 M KOH, Figure 3b) electrolytes. Herein, it should be mentioned that all of the laminated working electrodes were in a planar configuration and not subjected to any rotation (rotation speed of 0 rpm) during the electrochemical characterizations.
- (2) With the loading of NiO QDs as electrocatalysts, the *CNTR* electrodes exhibited further improvement in HER performances in both acidic (Figure 3a) and alkaline (Figure 3b) electrolytes. The performance of *NiO@CNTR* electrodes was found to be enhanced with the increasing catalyst (NiO QDs) loading, irrespective of the

Acid vs. Alkaline :: comparing HER activities at *NiO*@*CNTR* and *Pt* electrodes

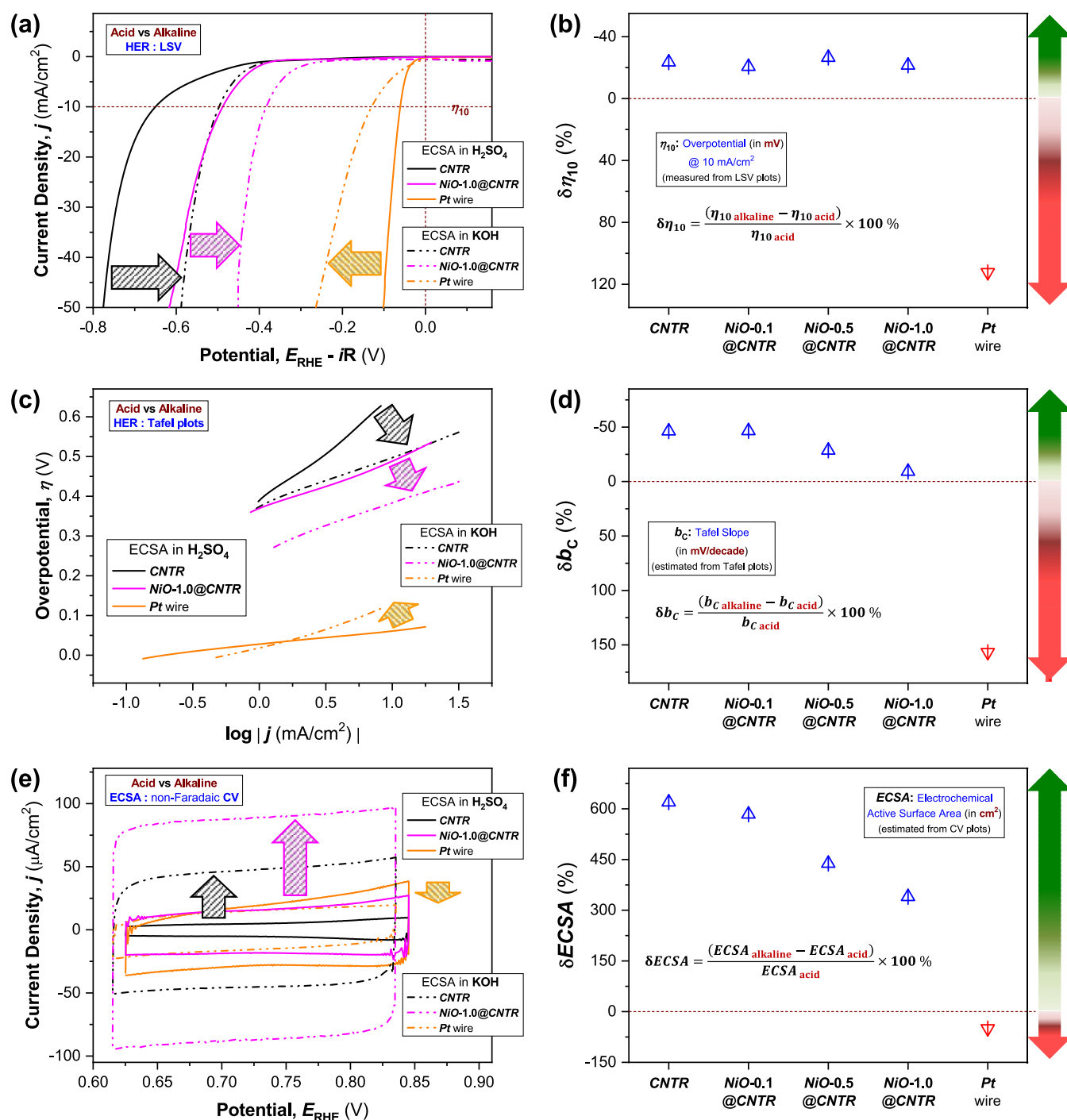


Figure 4. Acid vs alkaline electrolytes: HER activity. Comparison of HER performances of pristine (*CNTR*) and NiO QD-coated (*NiO-1.0@CNTR*) electrodes with a *Pt* wire in acidic (0.5 M H₂SO₄) and alkaline (1 M KOH) media: (a) LSV plots (iR corrected, at $\nu = 5$ mV/s) and corresponding (b) $\delta\eta_{10}$ values (change in η_{10} , overpotentials @ 10 mA/cm² value measured in alkaline media relative to that measured in acidic media). (c) Respective Tafel plots and corresponding (d) δb_c values (change in b_c , Tafel slopes). (e) CV plots performed in the non-Faradaic potential region (at $\nu = 50$ mV/s) and (f) estimated $\delta ECSA$ values (change in *ECSA*, electrochemical active surface area). The respective HER parameters achieved at other electrodes with various NiO QD loadings are also presented in panels (b, d, f). The green and red arrows, drawn at the right-side boundaries of panels (b, d, f) exemplify the direction of the “improvement” and “decline” of the HER performance, respectively.

electrolyte type, following the trend *NiO-1.0@CNTR* > *NiO-0.5@CNTR* > *NiO-0.1@CNTR*.

(3) Most interestingly, comparing Figure 3a,b, it can be revealed that both *CNTR* and *NiO@CNTR* electrodes

demonstrated a unique preference for the alkaline electrolyte, as evidenced by their improved HER activities obtained in a KOH solution compared to those measured in an acidic medium. For a clear picture, the HER

performances of *CNTR*, *NiO-1.0@CNTR* (with the highest NiO QD loading, *NiO-1.0*) electrodes, and the commercial *Pt* wire electrode are presented in Figure 4. Similar comparisons for other electrodes with varied NiO QD loadings are also demonstrated in Figure S5. As shown in Figure 4a, the LSV plots of the *CNTR* and *NiO-1.0@CNTR* electrodes in the alkaline electrolyte (1 M KOH) shifted further toward the theoretical HER potential, E^0 ($\text{H}_2\text{O}/\text{H}_2$) = 0 V, exhibiting significantly improved catalytic activities compared to that achieved in an acidic medium (0.5 M H_2SO_4). In comparison, the polarization curve of the *Pt* wire electrode shifted to a higher potential in KOH relative to that measured in H_2SO_4 , revealing degradation in HER activity from acid to alkaline electrolytes.

Detailed analysis of the LSV data, in terms of overpotential (η_{10} , required to achieve a current density of 10 mA/cm^2), disclosed that the η_{10} value of the *CNTR* electrode decreased by 24% ($\delta\eta_{10}$, defined by the equation shown in Figure 4b) from $\eta_{10 \text{ acid}} = 649.4$ mV (measured in acid, Table S2) to $\eta_{10 \text{ alkaline}} = 496.5$ mV (in alkaline, Table S3). Similarly, all of the *NiO@CNTR* electrodes also exhibited negative $\delta\eta_{10}$, as the acidic electrolyte was changed to alkaline. Notably, for the highest NiO QD loading (*NiO-1.0@CNTR* electrode), the η_{10} reduced from $\eta_{10 \text{ acid}} = 488.1$ mV (Table S2) to $\eta_{10 \text{ alkaline}} = 383.2$ mV (Table S3), resulting in the negative $\delta\eta_{10}$ ($\approx -22\%$), as shown in Figure 4b. Negative $\delta\eta_{10}$ is a measure of the “improvement” of HER activity (indicated by the green arrow drawn at the right boundary of Figure 4b). In contrast, positive $\delta\eta_{10}$ quantifies the “deterioration” of HER performance (directed by the red arrow, Figure 4b). In contrast, for the *Pt* wire, the trend was opposite (Figure 4b), with the η_{10} value increased by 112%, resulting in the positive $\delta\eta_{10}$ (Figure 4b), from 60.8 mV (in acid) to 129.1 mV (in alkaline), exhibiting sluggish HER activity of the *Pt* electrode in an alkaline electrolyte.

Furthermore, the Tafel analysis of the polarization curves, using eq S4, at low cathodic currents provided an important figure of merit, namely, the cathodic Tafel slope (b_c), a valuable indicator for probing the rate-determining step of HER and could be estimated directly from the linear fitting of the Tafel plots (Figure 4c, also Figure 3c,3d). Comparing the performance in acid (Figure 3c) versus alkaline media (Figure 3d), for both pristine and NiO QD-coated *CNTR* electrodes, the b_c values are found to reduce in KOH ($b_{c \text{ alkaline}} = 113$ mV/decade for *CNTR* and 95 mV/decade for *NiO-1.0@CNTR*) relative to that measured in H_2SO_4 (Table S2, $b_{c \text{ acid}} = 211$ and 104 mV/decade, for *CNTR* and *NiO-1.0@CNTR* electrodes, respectively), leading to the negative values of δb_c (46 and 9%, respectively), as observed in Figure 4d. Similar to the trend of $\delta\eta_{10}$, a negative δb_c represents faster and favorable HER kinetics, indicating an enhanced HER activity of the *CNTR* and *NiO@CNTR* electrodes in an alkaline medium. Predictably, the *Pt* wire electrode becomes a poor electrocatalyst exhibiting much higher b_c in KOH (87.9 mV/decade) than in H_2SO_4 (34.2 mV/decade), resulting in a positive δb_c of over 150% (Figure 4d).

The enhancement in active site density is another critical indicator of a favorable HER activity, which could be quantified by estimating the effective electrochemically active surface area (ECSA) of the HER electrodes (eq S5), derived from the respective double-layer capacitance (C_{dl} , eq S6) and measured via conducting cyclic voltammograms (CV) in a non-Faradaic

potential region at various potential scan rates (ν) following McCrory et al.'s methodology.⁴⁸ Figure 4e represents a comparison between the CV plots (at $\nu = 50$ mV/s) measured in acid and those performed in alkaline media for *CNTR*, *NiO-1.0@CNTR*, and the *Pt* wire. The detailed comparison of CV scans for all of the electrodes is shown in Figure S6a (acid electrolyte) and Figure S6b (alkaline electrolyte). The respective C_{dl} values were averaged from the slopes of the linear plots of cathodic (i_c) and anodic current (i_a) as the function of ν , measured in acid (Figure S6c) and alkaline (Figure S6d) media, respectively. Interestingly, all of the *CNTR* and *NiO@CNTR* electrodes exhibited a higher C_{dl} , hence higher ECSA values in alkaline media (Table S3), compared to those achieved in an acidic electrolyte (Table S2). The calculated δECSA shows positive values for both *CNTR* ($\approx 620\%$) and *NiO@CNTR* electrodes ($\approx 340\%$ at *NiO-1.0@CNTR*), whereas it shows a negative value for the *Pt* wire electrode ($\delta\text{ECSA} \approx -50\%$), as shown in Figure 4f. Opposite to the trends of $\delta\eta_{10}$ and δb_c , the δECSA becomes positive for an enhanced HER activity, while a negative δECSA signifies a loss of HER activity due to a reduction in ECSA.

2.3.2. Alkaline-Friendly Nature of *CNTR* and *NiO@CNTR* Electrodes. Such contrast between the *CNTR* electrodes (pristine and NiO QD-coated) and *Pt* electrodes can only be explained by the difference in HER kinetics and pathways in H_2SO_4 and KOH. As per the classical theory of cathodic HER,⁴⁹ there are two possible reaction pathways that can be adopted, namely Volmer–Tafel (VT) and Volmer–Heyrovsky (VH). First, the adsorption of intermediate adsorbed hydrogen atoms (H_{ads}) on the cathodic (working) electrode surface occurs via the Volmer reaction, through eq S1a in acidic or eq S1b in alkaline media.^{33,50} The next and final step would follow either the Heyrovsky desorption (via a reaction of H_{ads} intermediates with proton, eq S2a,b) or the Tafel desorption (via recombination of the two H_{ads} , eq S3) to generate a H_2 gas molecule.

The source of protons varies depending on the type of the electrolyte and plays a pivotal role in initiating the HER kinetics. In acidic media, the source of protons is H_3O^+ , which directly initiates the HER (Volmer step, eq S1a). But in alkaline media, the source of protons is no longer H_3O^+ but simply H_2O , the dissociation of which first takes place via eq S1b, producing the oxygen species (OH^-) at the electrode/electrolyte interface.^{33,50}

In acidic media, being a noble metal, the *Pt* electrode can easily facilitate the Tafel step (eq S3) directly after the Volmer step, following the VT pathways for HER, which is also evidenced by its b_c value close to 30 mV/decade (satisfying the condition for the Tafel reaction being the rate-determining step). However, in alkaline media, the production and adsorption of OH^- moieties at the Pt–electrolyte interface (eq S1b) impede the catalyzing capability¹⁷ of Pt toward the cleavage of the H–OH bond,⁵¹ decelerating the overall HER kinetics.⁵² Evidently, the b_c value of 87.9 mV/decade also suggested that the HER kinetics at the *Pt* wire electrode in KOH followed the VH reaction pathways¹⁷ (eq S1b followed by eq S2b).

On the contrary, in both acidic and alkaline media, the *CNTR* and *NiO@CNTR* electrodes followed the VH pathways, exhibiting high b_c (>40 mV/decade) values, with the Heyrovsky reaction as the rate-determining step. However, as observed in Figure 4d, in alkaline media, the b_c values are found to reduce substantially relative to those measured in acidic media, leading to the negative values of δb_c and suggesting the escalation in the

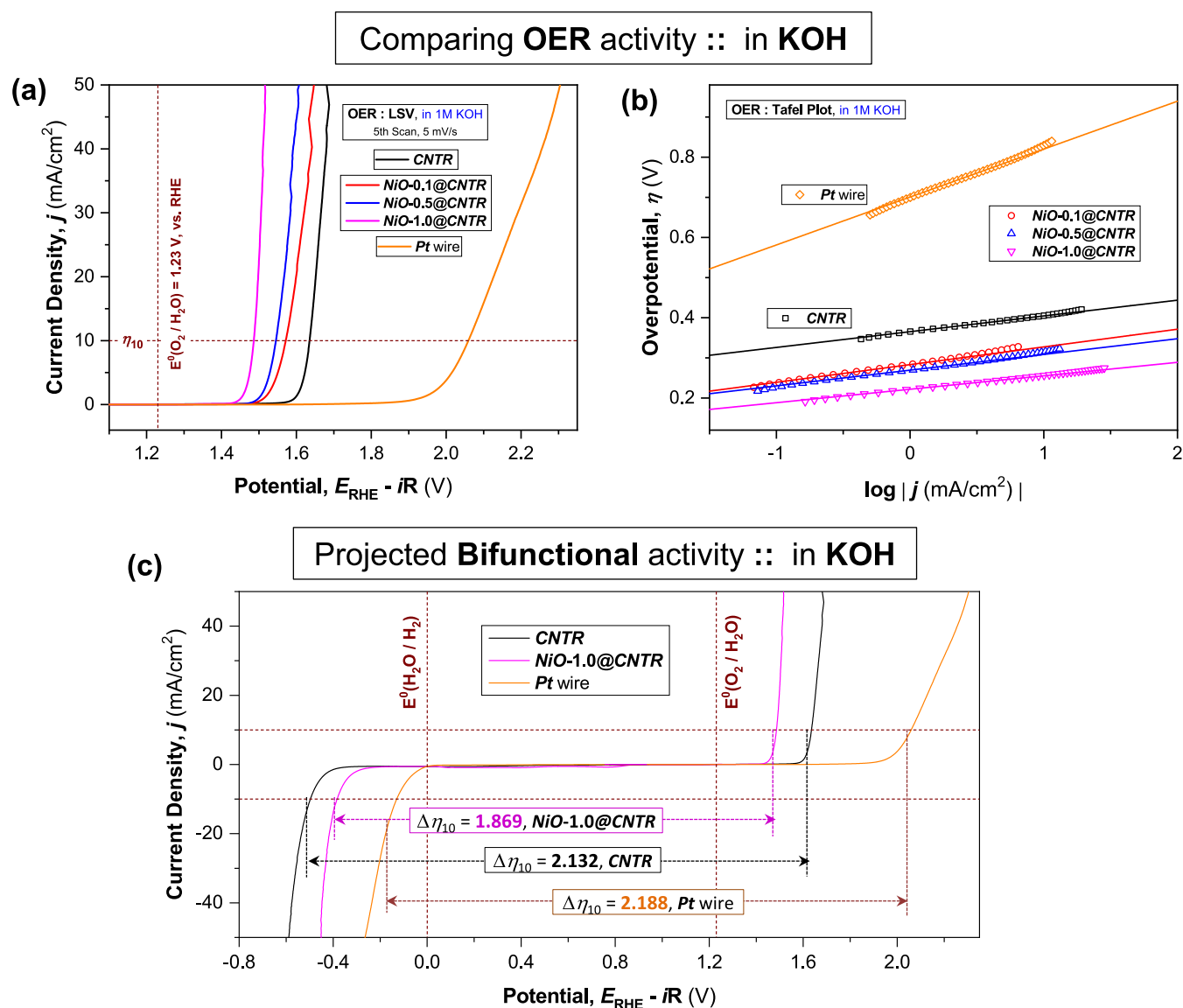


Figure 5. Oxygen evolution reaction (OER) and bifunctional activity. (a) OER activity of *CNTR* and *NiO@CNTR* electrodes in a N_2 -saturated alkaline medium (1 M KOH), at $\nu = 5$ mV/s, without any rotation of the working electrode. (b) Corresponding Tafel plots of overpotential (η) vs $\log(j)$ measured in 1 M KOH; all potentials were presented after iR correction. Respective data measured at the commercial *Pt* wire electrode are presented for comparison. (c) Projected bifunctional activity of *CNTR* and *NiO-1.0@CNTR* electrodes: values of full-cell potential $\Delta\eta_{10}$ estimated from the difference between overpotential values (η_{10} , estimated at ± 10 mA/cm²) achieved from the respective HER and OER polarization curves (recorded in 1 M KOH), with the *Pt* wire as a reference for comparison.

reaction rate and alkaline-friendly nature of *CNTR* and *NiO@CNTR* electrodes.

The OH^- moieties, associated with alkaline HER, interact favorably with the extended graphitic domains³⁴ obtained from the hexagonal walls of CNT components of the *CNTR*. Concurrently, the presence of inherent oxygen moieties (COOH, C–O, C=O and O–C=O, as evidenced by the XPS study, Figure 1f) on the *CNTR* surface favors the adsorption and dissociation of H_2O molecules, efficiently initiating the HER process. Also, the same oxygen moieties could increase the supply of OH^- groups³³ and other supportive H–OH species³⁴ at the electrode/electrolyte interface, promoting the HER rate (Figure 4a,4b). In addition, our *CNTR*, being a 3D ensemble of randomly oriented nanotubes, also provides a disordered carbon surface exposing an abundant density of catalytic sites,³³ as evidenced by the significant

enhancement of its *ECSA* value in KOH compared to that obtained in H_2SO_4 (Figure 4e).

As for the *NiO@CNTR* electrodes, it can be suggested that *NiO* QDs and *CNTR* would work in concert, where the oxophilic power of *NiO* QDs and existing oxygen moieties on the *CNTR* surface favor the adsorption and dissociation of H_2O molecules. At the same time, synergistically, the adjacent C atoms (the graphitic domains) provide the active sites for the enhanced recombination of H_{ads} intermediates.^{5,6,13,51,53} Here, the “synergistic coupling” arises from the good adhesion with an improved interface between the *NiO* QDs and *CNTR* surface, which works in complement to each other for maintaining the uninterrupted chemical reaction steps, accelerating the preferred catalytic reactions and leading to a desired long-term stability in the catalytic performances. Such a “synergistic effect”^{5,6} has also been reported in earlier studies involving hybrid electrocatalysts,

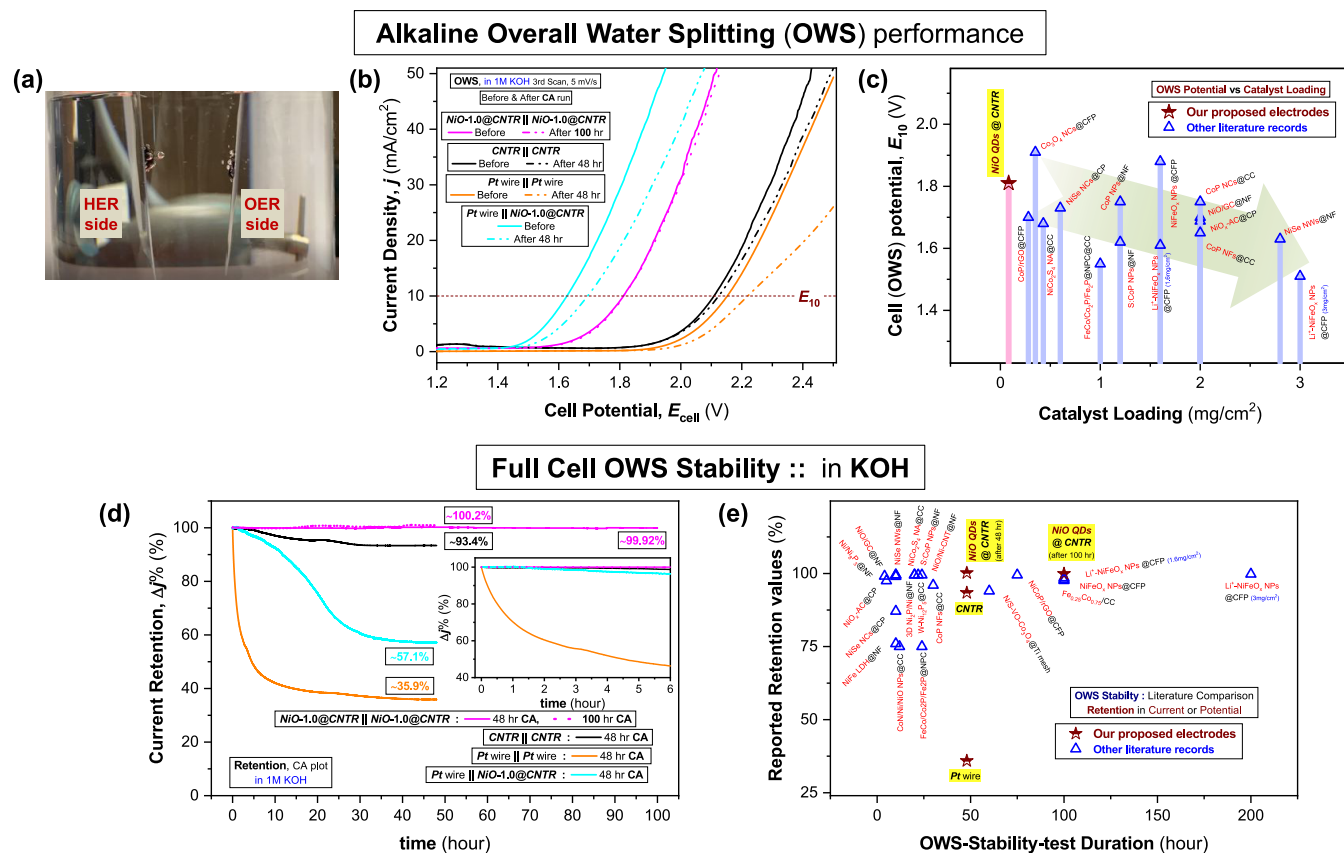


Figure 6. Bifunctional catalytic activity of *CNTR* and *NiO-1.0@CNTR* electrodes using the same electrode materials as both the anode and the cathode in a two-electrode (2E) alkaline electrolyzer cell. (a) Digital image of the experimental setup during the overall water-splitting (OWS) performances (of the *NiO-1.0@CNTR* || *NiO-1.0@CNTR* electrolyzer) in a N_2 -saturated alkaline medium (1 M KOH). (b) Polarization (OWS, without iR correction) plots for *CNTR* || *CNTR* and *NiO-1.0@CNTR* || *NiO-1.0@CNTR* electrolyzers with the *Pt* wire || *Pt* wire as a reference for comparison; at $\nu = 5$ mV/s: comparison of LSV plots measured before and after the stability test (presented in panel (d)). For comparison, an asymmetric cell configuration (*Pt* wire || *NiO-1.0@CNTR*) was also presented, using the *Pt* wire as a cathode and *NiO-1.0@CNTR* as an anode. (c) Brief literature comparison of the reported OWS cell potential (E_{10}) as a function of the respective catalyst loading, as reported for various bifunctional electrocatalysts in 1 M alkaline electrolytes (KOH or NaOH). (d) Long-term stability of OWS (chronoamperometry, CA), monitoring the current retention at the respective E_{10} (recorded at a current density of 10 mA/cm² from the initial OWS plots (before CA measurement, panel (b))). The inset represents the respective current retention during the first 6 h. All of the electrolyzers were subjected to a 48 h CA study. Only, for our proposed electrodes, the performance of the *NiO-1.0@CNTR* || *NiO-1.0@CNTR* electrolyzer was repeated (using a fresh set of electrodes) for a more extended stability study for 100 h. (e) Brief literature comparison of OWS stability performance of various bifunctional electrocatalysts reported in 1 M alkaline electrolytes (KOH or NaOH), displaying the reported current (or potential) retention values in the stability-test duration scale.

such as NiO electrocatalysts on metallic support⁵³ or Ni/NiO catalysts.^{13,51}

2.3.3. Oxygen Evolution Reaction (OER) and Bifunctional Activity. To realize the bifunctional nature of the proposed electrodes being appropriate for the overall water-splitting application, the OER performances of the *CNTR* and *NiO@CNTR* electrodes were also evaluated in N_2 -saturated 1.0 m KOH (Figure 5a). The *CNTR*, without any additional catalysts loading, displayed a substantially superior performance ($\eta_{10} \approx 1.635$ mV and $b_A \approx 39.2$ mV/decade) relative to the *Pt* wire electrode ($\eta_{10} \approx 2.059$ mV and $b_A \approx 119.4$ mV/decade, Table S4). With the loading of NiO QDs, the *NiO@CNTR* electrodes exhibited further improvement in OER performances, lowering both η_{10} and b_A (anodic Tafel slope, Figure 5b) values as the NiO QD loading increases. The *NiO-1.0@CNTR* electrode exhibited the best catalytic activities of O_2 generation, with η_{10} of 1.486 mV and b_A of 33.5 mV/decade in an alkaline electrolyte (1 M KOH, Table S4).

Compared to HER, the OER mechanism is comparatively more complicated and less clarified in the literature.^{52,54} In a

simple view, OER follows a $4e^-$ pathway (eqs S8–S11) in alkaline media, initiated with the hydroxide (OH^-) anion and associated with the adsorption of O_{ads} intermediates. Hence, based on the earlier arguments for the alkaline-HER activity, it can be reasonably anticipated that the *Pt* wire electrode will suffer from sluggish OER activity. In contrast, both the *CNTR* and *NiO@CNTR* surfaces could readily favor the adsorption of both OH^- and O_{ads} intermediates, accelerating the subsequent reaction steps and displaying a significantly superior OER activity compared to the *Pt* counterpart.

On the basis of the above-mentioned studies, it can be rationally predicted that both *CNTR* and *NiO@CNTR* electrodes would be excellent bifunctional catalysts for HER and OER in alkaline media. As shown in Figure 5c, replotting both cathodic (HER) and anodic (OER) polarization curves, collected by three-electrode configuration, the potential difference ($\Delta\eta_{10}$) between HER and OER current density (of 10 mA/cm²) for *CNTR*, *NiO-1.0@CNTR*, and *Pt* wire electrodes represent an expected full-cell potential window. The calculated values of full-cell potential $\Delta\eta_{10}$, the difference between the

overpotential values (at ± 10 mA/cm²) achieved from the relevant HER and OER polarization curves, are 1.869, 2.132, and 2.188 V, for NiO-1.0@CNTR, CNTR, and Pt wire, respectively. These values clearly signify the superior performance of NiO-1.0@CNTR compared to that of the Pt wire, suggesting its potential application for a practical overall water-splitting (OWS) device in an alkaline electrolyte, employing the same electrode materials as both the anode and the cathode.

2.4. Bifunctional Catalytic Performance for Alkaline Overall Water Splitting (OWS). The OWS performance was assessed by assembling the same electrode materials as both the anode and the cathode in a two-electrode (2E) alkaline electrolyzer cell (Figure 6a, also find the Supporting Video SV2_OWS). In Figure 6b, the polarization curve (without *iR* correction) of the NiO-1.0@CNTR || NiO-1.0@CNTR electrolyzer exhibits a cell potential (E_{10}) of ~ 1.81 V (recorded at a current density of 10 mA/cm²), significantly better than that obtained with the Pt wire || Pt wire electrolyzer. Interestingly, the CNTR || CNTR electrolyzer also exhibited an excellent OWS performance with an E_{10} of 2.11 V, better than that of the Pt wire || Pt wire electrolyzer ($E_{10} \approx 2.15$ V). In this study, we employed the OWS performance of the Pt wire only as a “reference” for the comparative study with our proposed electrodes, as it is commonly used for comparison and sometime considered as a benchmark material for such catalysis application specifically for HER. The water-splitting potential (E_{10}) values obtained from the 2E electrolyzer (in symmetric cell configuration) are lower than the predicted full-cell potential $\Delta\eta_{10}$ values calculated, as shown in Figure 5c, which imply benefits from the effective integration of OWS devices using the same electrode materials as both the anode and the cathode. For comparison, an asymmetric cell configuration (Pt wire || NiO-1.0@CNTR) was also presented, using the Pt wire as a cathode and NiO-1.0@CNTR as an anode, which exhibited excellent OWS performance with an $E_{10} \approx 1.63$ V (Figure 6b), slightly higher than the predicted $\Delta\eta_{10}$ value obtained, as shown in Figure 5c. However, as observed and discussed later, such asymmetric cell configuration cannot provide adequate stability in long-term OWS performance because of the degradation of Pt metal in an alkaline medium.

As compared with other materials available in the literature (see Table S5, in SI), our bifunctional NiO-1.0@CNTR electrode exhibited a promising OWS potential (E_{10} of ~ 1.81 V), with the minimal loading of the NiO QD catalyst (≈ 83 $\mu\text{g}/\text{cm}^2$ only), which is comparable to the E_{10} values reported in other single (transition) metal-based bifunctional catalysts with at least 1 order of magnitude higher “catalyst loading”,^{10,14,15,44–46,55–61} such as NiO nanosheets (NSs) on a nickel foam or NF ($E_3 > 1.8$ V with a loading of 0.53 mg/cm²),⁵⁸ α -NiOOH NSs on NF ($E_4 > 1.75$ V with 0.74 mg/cm² loading),⁵⁸ NiO/GC on NF ($E_{10} \sim 1.7$ V with 2 mg/cm² loading),⁵⁹ NiO_x-AC on carbon paper or CP ($E_{10} \sim 1.69$ V with 2 mg/cm² loading),⁶⁰ Ni(OH)₂ NSs on NF ($E_{10} \sim 1.82$ V),¹⁵ Co₃O₄ nanocrystals (NCs) on carbon fiber paper or CFP (1.91 V with 0.35 mg/cm² loading),⁴⁶ Ni_{0.5}SellNi_{0.75}Se NCs on CP (1.73 V with 0.6 mg/cm² loading),⁴⁴ W-Ni₁₂P₅ on carbon cloth or CC (1.73 V),⁶¹ CoP NCs on CC (1.75 V with 2 mg/cm² loading),⁵⁵ and CoP NPs on NF (1.75 V with ~ 1.2 mg/cm² loading).¹⁴ Figure 6c presents a graphical comparison of the “ E_{10} ” values for various bifunctional electrocatalysts reported in the past literature as a function of the respective “catalyst loading”. The literature comparison (Table S5 and Figure 6c) also presents several reports of lower E_{10} values, which are

mainly reported for the bimetallic or hybrid catalyst systems^{13–16,43,47,62–66} and the catalysts with much higher loading compared to our work;^{10,13,16,47,55} for example, NiFe layered double hydroxides on NF (1.7 V),¹⁵ S-doped CoP NPs on NF (1.62 V with ~ 1.2 mg/cm² loading),¹⁴ CoN/Ni/NiO NPs on CC (1.56 V),⁶³ Fe_{0.25}Co_{0.75} on CC (1.66 V),⁶⁴ NiCo₂O₄ nanowires (NWs) and NiCo₂S₄ NW-array on carbon cloth (1.98 and 1.68 V, respectively, with 0.43 mg/cm² loading),⁴³ NiFeO_x and Li⁺-NiFeO_x nanoparticles on carbon fiber paper or CFP (1.88 and 1.61 V, respectively, with ≈ 1.6 mg/cm² loading),¹⁶ 3D Ni₂P/Ni on NF (1.49 V),⁶⁵ NiCoP/rGO on CFP (1.59 V with ~ 0.15 mg/cm² loading),⁶⁶ NiO/Ni-CNT||NiFe LDH on NF (1.41 V with ~ 8 mg/cm² loading),¹³ or Ni/Ni₃P₃ on NF (1.61 V with ~ 10.5 mg/cm² loading).⁴⁷

While comparing the performance of our NiO@CNTR electrode with the literature, it is also worth emphasizing the simple, rapid, and scalable fabrication process (spray-coating) of our proposed electrode. Core catalysts, the PiNE-synthesized NiO QD colloids have the advantage of a single-step synthesis process with no further purification needed; also, the particle size remains stable for a long time (years), and no agglomeration happens with no surfactant needed. At the same time, from the viewpoint of the CNTR matrix, there is no length limitation in producing CNTR as long as the precursor feed is available and the material remains mechanically and chemically stable without any need for specific storage. Moreover, the macroscopic form of CNTR is easily formable to various shapes and sizes, which is an added advantage for customized fabrication of electrodes. This gives a competitive advantage to our electrode for easy transfer of this technology to an industrial scale for practical applications.

The stability or durability of the electrodes was assessed by using chronoamperometry (CA, Figure 6d), maintaining the respective cell potential (E_{10} , recorded at a current density at 10 mA/cm² from the initial OWS plot, Figure 6b). Impressively, the NiO-1.0@CNTR || NiO-1.0@CNTR electrolyzer reported in this study is found to retain the initial current density even after 4 days, which shows the current retention of $\approx 100.2\%$ after 48 h and $\approx 99.92\%$ after 100 h of electrolysis operation, as shown in Figure 6d, suggesting a promising performance of the NiO@CNTR electrode for a prolonged OWS run. Interestingly, the CNTR || CNTR electrolyzer also exhibited high stability in current (losing only $\sim 6\%$ of the initial value) over 48 h of continuous run (Figure 6d). Relatively, the Pt wire || Pt wire electrolyzer retained only 36% of the initial current after the stability test of 48 h (Figure 6d). Furthermore, we tested the reproducibility of our results by repeating the stability test for the Pt wire||Pt wire and CNTR||CNTR electrolyzers for two different sets of electrodes, as shown in Supporting Figure S7. Notably, as mentioned earlier, the Pt wire || NiO-1.0@CNTR asymmetric electrolyzer also failed to maintain reasonable stability, retaining only $\sim 57\%$ of the initial current density after 48 h run. These findings would justify our quest for a “bifunctional” electrode that can catalyze both HER and OER, leading to a simple and symmetric cell configuration with stable and effective OWS performance. Besides, configuring the electrolyzer cell with the same materials for both electrodes (cathode and anode) would help to avoid the complexity of using different electrodes for HER and OER and unwanted “contamination” of electrodes and electrolytes. A comparative study^{10,13–16,43,44,47,55,56,59–66} of current (or potential) retention over time, as reported in a previous literature, is shown in Figure 6e, which indicates the superior nature of our electrodes in terms of long-standing stability for OWS application.

“Long-term” stability in the current acquired with slight reduction and subsequent growth cycles implies a self-healing nature of the catalysts, originating from the “synergistic coupling”^{5,6} between NiO QDs and the CNTR matrix. Earlier reports¹⁶ justified such “long-standing stability” as an outcome of the “slow” adsorption/desorption kinetics of the reaction intermediates that happened at the catalyst’s sites (e.g., NiO QDs). With time, as the reaction proceeds, the adsorbed intermediates impede the electrolyte diffusion to the catalyst sites, slowing down the next reaction steps. However, the slow kinetics would provide sufficient time for the neighboring active sites (e.g., C or Ni⁰) to facilitate the desorption step, consequently refreshing the surfaces and boundaries of the interconnected particles.¹⁶ Such a course of “self-healing” action would, in turn, recover the catalytic activity, regaining the current to its initial value.^{5,6} In addition, the “slow” formation of gas bubbles leads to a gradual growth of bubbles adhered to the electrodes’ surface (please find the [Supporting Video SV2_OWS](#) displaying the phenomenon during the OWS run), hindering effective contact with the electrolyte and resulting in a decline of reaction. As the bubbles grow to a limit, sudden release of bubbles (H₂ and O₂ gases) from the surface of electrodes (cathode and anode, respectively) would occur in periodic intervals, which could also help remove surface residues and contribute to the undulating activation process observed.^{13,16}

The LSV measurements before and after the stability (CA) test (Figure 6b) reveal that our proposed NiO-1.0@CNTR || NiO-1.0@CNTR electrolyzer exhibited a repetitive LSV plot maintaining the initial OWS performance even after 100 h of run, as evidenced in Figure 6b, suggesting a favorable utilization of the NiO@CNTR electrode for a long-term OWS application. Interestingly, the pristine CNTR || CNTR electrolyzer exhibited a minor degradation in OWS performance after a 48 h stability test. Comparatively, the LSV performances of the Pt wire || Pt wire and Pt wire || NiO-1.0@CNTR electrolyzers suffered heavily after the stability test of 48 h (Figure 6b).

3. CONCLUSIONS

This study successfully demonstrates the bifunctional electrocatalytic activity of a novel electrode, NiO@CNTR, by hybridizing macroscopically assembled carbon nanotube ribbons (CNTRs, directly spinning from the CVD reactor) and NiO QDs (synthesized by PiNE) for efficient and highly stable alkaline-based OWS applications. The comparison of HER activities in different electrolytes revealed that the proposed electrodes strongly prefer the alkaline media over the acidic one, as evidenced by the lowering of η_{10} and b_C parameters and enhancement of ECSA. In contrast, the noble metal catalyst (here, a Pt wire electrode) exhibited a considerable degradation in HER activity in an alkaline electrolyte, as substantiated by the increase in η_{10} and b_C and the decrease in ECSA, compared with its acidic HER. Collectively, in a 2E configuration for alkaline electrolysis, by assembling the same electrode materials as both the anode and the cathode for HER and OER, superior performance of NiO@CNTR relative to Pt was observed. Furthermore, this superior performance of our proposed NiO@CNTR electrode has been achieved with a very low NiO QD loading (only 83 $\mu\text{g}/\text{cm}^2$) compared to other loading values reported in the literature for various bifunctional electrocatalysts. NiO@CNTR exhibited a cell potential of only 1.81 V at 10 mA/cm² for OWS, which is much lower than that of the Pt wire ($E_{10} \approx 2.15$ V). It also

demonstrated remarkable catalytic activity accompanied by “long-term” OWS stability, retaining $\sim 100\%$ of the initial current after a 100 h long OWS run. The superior performance of NiO@CNTR is mainly attributed to the alkaline-friendly and bifunctional nature of both the NiO QDs and the CNTR support as well as the synergistic coupling between them. This proposed NiO@CNTR electrode with high chemical and mechanical stability can provide a viable solution for fuel cell technology as the material synthesis and electrode fabrication process involve simple and scalable techniques by avoiding any requirement of a surfactant, a binder, and complex purification steps. This study also shows a pathway toward cost-effective and large-scale sustainable solutions for electrochemical water-splitting devices, which can be used as an alternative energy source with limited environmental effects.

4. EXPERIMENTAL SECTION

4.1. Chemicals. All analytical grade chemicals were purchased and used without any further purification process. Ferrocene (Fe(C₅H₅)₂, $\geq 98\%$), thiophene (C₄H₄S, $\geq 99\%$), sulfuric acid (H₂SO₄, 95–98%), and potassium hydroxide (KOH, $\geq 90\%$, flakes) were purchased from Sigma-Aldrich. Pure methane and hydrogen gases (BOC, UK) were used as the reactant gas during the growth of CNTR by the thermal CVD technique. A Ni foil of 99.5% purity (GoodFellow) was used as an anode as well as the Ni source in the PiNE synthesis. Commercial Pt wires (99.95% purity) were purchased from BASi and used as counter electrodes for HER and OER tests. Milli-Q water, with a resistivity of ≈ 15 M Ω /cm, was used to prepare all solutions (PureLab option, UK).

4.2. Synthesis of CNT Ribbons (CNTRs). CNTRs were synthesized using a floating catalyst-assisted thermal CVD technique.^{20,22,23} For the synthesis, methane was used as a carbon precursor, and an iron (Fe) floating catalyst was obtained by decomposing ferrocene at high temperature. At a temperature above 400 °C, ferrocene starts to break down and releases Fe atoms. The aggregation of Fe atoms eventually leads to the formation of Fe nanoparticles (NPs), which serve as catalytic sites for the growth of CNTs. Hydrogen was used as a promoter/carrier gas during the CVD synthesis of the CNTs. Carbon atoms rearrange to form CNTs on the surface of catalyst NPs, collectively forming a macroscopically assembled CNT network, which can be extracted from the furnace onto a moving winder (Figure S1a,b).

Following our earlier publication by Brunet et al.,²⁰ the synthesis of the CNT aerogel was performed under a methane flow rate of 160 sccm and a carrier hydrogen flow rate of 1350 sccm through a tube furnace held at 1290 °C. For the formation of Fe NP catalysts, the ferrocene and thiophene supplies were maintained by a carrier H₂ flow with rates of 130 and 90 sccm, respectively. Figure S1c,d represents a typical as-synthesized 3D ensemble of a randomly oriented CNT network (also Figure 1b).

Prior to any characterization or application, the as-synthesized macroscopic CNT network was further processed by pressing it between two glass microscope slides for a few (3–5) minutes under an applied force of ≈ 18 N to form a flat and compact fabric-like material (Figure 1c,d). Supporting Figure S1e–k reveals the flexible and lightweight nature of a typical CNTR (also see the Supporting Video SV1_CNTR). Depending on the compressive force applied, the thickness of the CNTR sample can be tailored. In this study, the CNTR thickness was maintained between 3 and 5 μm (Figure 1e). The material (CNTR) and its synthesis process were extensively characterized in our previous publication.²⁷

4.3. Synthesis of NiO Quantum Dots (QDs). NiO QDs with a narrow size distribution were synthesized using PiNE,^{26,35–37} as demonstrated in the digital image (Figure S4a) and the schematic diagram (Figure S4b) of the experimental setup. Similar to our earlier publication by Chakrabarti et al.,²⁶ a nickel foil of a 99.5% purity (Goodfellow Cambridge Ltd.) was used as an anode as well as the Ni source in the synthesis. A nickel tube (0.7 mm internal diameter and 1 mm outer diameter) was used as the cathode; the distance between the

anode and the cathode was kept constant at about 1.8 cm. Pure He gas was flown at a flow rate of 50 sccm through the nickel tube, and an initial voltage of 3 kV was used to initiate the plasma between the end of the nickel tube and the surface of the ethanol. For each synthesis batch, 15 mL of ethanol was used, the immersed area of the Ni foil was maintained at 1.5 cm × 1.5 cm, and the distance between the nickel tube and the surface of the liquid was kept at 2 mm.

For igniting the plasma, a direct current (DC) voltage of 3 kV was applied and set until the current reached 5 mA. Then, the current was maintained constant (around 5 mA) by gradually decreasing the voltage from 3 to 2 kV. A total deposition time of 45 min was retained for each synthesis of NiO QDs with an intermediate pause of 2 min at each 10 min interval.

4.4. Deposition of NiO QDs on CNTR. For fabrication of NiO QD-coated CNTR electrodes (*NiO@CNTR*), the PiNE-synthesized NiO QD-ethanol colloids were spray-coated onto the laminated CNTR electrodes at three different volume concentrations, roughly 66 μg/mL (as-synthesized colloids, symbolized as *NiO-1.0*), ≈33 μg/mL (two times diluted, *NiO-0.5*), and ≈6.6 μg/mL (diluted by ten times, *NiO-0.1*). Detailed spray-coating parameters and NiO QD loading concentration are given in Table S1. In summary, three *NiO@CNTR* electrodes, namely *NiO-1.0@CNTR*, *NiO-0.5@CNTR*, and *NiO-0.1@CNTR*, were loaded by 83 μg/cm², 42 μg/cm², and 8.3 μg/cm² of NiO QDs, respectively. For comparison, the pristine CNT ribbon was also employed as an electrode (*CNTR*), representing its electrocatalytic activity without any additional catalysts.

4.5. Fabrication of Laminated Electrodes of Pristine and NiO QD-Coated CNTR. For electrode preparation, the as-synthesized CNT ribbon (Figure 1d) was cut into desired pieces, and those CNTR pieces were manually interlaced with adhesive copper tape and nickel conducting paste. The Cu tape (and Ni conducting paste) is used only to extend the electrical contact for the current collection. Finally, the assembly was laminated, maintaining a window (only on one side of the laminate) for the exposure of CNTR (only) to the electrolyte. The circular window represents the active area (0.45 cm diameter) of our laminated electrodes for electrochemical reaction, as shown in Figure S3a.

4.6. Material Characterizations and Instrumentation. SEM images of the samples were obtained with a JEOL JSM-6010PLUS operating at a 20 kV acceleration voltage. For the TEM measurements, the JEOL JEM-2100F system equipped with a field-emission electron gun operated at 200 kV was used. Energy dispersive spectroscopic (EDS) measurements were carried out using an OXFORD 80 mm² X-Max Silicon drift detector fitted onto the TEM. The software from INCA was used to analyze the data. EELS measurements were carried out in the scanning TEM mode using the integrated GATAN Enfium spectrometer. X-ray photoelectron spectroscopy (XPS) was used to analyze the chemical composition of the materials. An X-ray source (Al = 1486 eV) with a spot size of 400 μm² was used with a Kratos Axis Ultra DLD spectrometer. The sample analysis chamber pressure was maintained at 10⁻⁹ bar for all measurements. During the measurements, the operating current and voltage were 10 mA and 15 kV, respectively. Specific region scans were performed at a resolution of 0.05 eV and a pass energy of 20 eV. The obtained spectra were calibrated using the C 1s peak located at 284.5 eV. Raman spectroscopy was used to acquire experimental information about the electronic and vibrational properties of the CNTs and was carried out using a Horiba Labram 300 Raman spectrometer, using a HeNe (633 nm) laser for excitation.

Prior to any basic characterizations (SEM, Raman and XPS studies), a tiny piece of CNTR was laid down onto a silicon substrate. Several drops of ethanol were applied and evaporated at an elevated temperature, resulting in a dry ribbon that adhered to the silicon substrate. TEM samples of CNTR samples were prepared using a minute piece of CNTR (collected by tweezers) on a holey carbon-coated copper grid of 300 meshes, followed by dropping a few microlitres of ethanol and subsequently drying overnight. For the NiO QDs, diluted ethanol-dispersed NiO QDs were drop-cast on a silicon substrate and dried under an elevated temperature before SEM and XPS studies. TEM samples were prepared by dropping 1 μL of ethanol-dispersed NiO QDs on a holey lacey carbon-coated (300 mesh) copper

grid and dried under incandescent lamp light radiation for 5 min. Then, the grid was kept at room temperature for a few hours with a glass protection cover.

4.6.1. Electrochemical Studies. All electrochemical studies were carried out using a BioLogic potentiostat, SP-200 (Bio-Logic Science Instruments Ltd., UK), coupled with an EIS channel. A typical three-electrode system (Figure S3b) was used to examine the activity of the proposed pristine *CNTR* and *NiO@CNTR* laminated electrodes (Figure S3a), used as the working electrode. A platinum wire (99.95% purity, BASi) and Ag/AgCl (3 M KCl, BASi) were used as counter (CE) and reference electrodes (RE), respectively. In addition, a commercial Pt wire (99.95%, BASi) was also purchased from BASi and used as a reference working electrode for HER and OER tests.

Two (aqueous) electrolyte solutions, 0.5 M H₂SO₄ (pH = 0.29) and 1 M KOH (pH = 14.0), were freshly prepared and subjected to the N₂ gas purging for hours to remove the dissolved oxygen. Before conducting the HER or OER activity studies, all of the working electrodes were preconditioned by cyclic voltammetry (CV) at a potential scan rate (ν) of 100 mV/s for at least 20 scans.

The polarization studies were carried out by employing linear sweep voltammetry (LSV) at ν of 5 mV/s. Herein, it should be mentioned that all of the laminated working electrodes were in a planar configuration, not subjected to any rotation (rotation speed of 0 rpm). All of the electrochemical experiments were conducted at room temperature (20 ± 2 °C).

All of the measured potentials were converted to a reversible hydrogen electrode (RHE) using the Nernst equation: $E_{\text{RHE}} = E_{\text{Ag/AgCl}} + (0.059 \times \text{pH}) + E_{\text{Ag/AgCl}}^0$ (where, $E_{\text{Ag/AgCl}}^0 = 0.210$ V at 25 °C). The pH values of 0.5 M H₂SO₄ and 1 M KOH are estimated as 0.29 and 14.0, respectively. Furthermore, all of the potentials in the reported cathodic (HER) or anodic (OER) polarization curves (LSV plots) were corrected for ohmic losses (iR drop correction) manually by using AC-impedance solution (or electrolyte) resistance (R_s).

The double-layer capacitance (C_{dl}) was estimated by performing the CV in the non-Faradaic potential region at different scan rates ($\nu = 10, 20, 30, 40, 50, \text{ and } 60$ mV/s). The C_{dl} value was averaged from the anodic and cathodic slopes of the linear plots of anodic (i_A) and cathodic current (i_C) versus the potential scan rate (ν), respectively.

■ ASSOCIATED CONTENT

Supporting Information

The Supporting Information is available free of charge at <https://pubs.acs.org/doi/10.1021/acsami.3c12944>.

Equations used to calculate the measured parameters; figures for the supporting studies; and tables for the numerical analysis of electrocatalytic data (PDF)

Flat and compact fabric-like CNTR after compression revealing its flexible and lightweight nature (Supporting Video SV1_CNTR) (MP4)

Bifunctional catalytic activity of NiO QD-coated CNTR electrodes, employing as both the anode and the cathode in a 2E configuration, for the OWS performances in a N₂-saturated alkaline medium (SV2_OWS) (MP4)

■ AUTHOR INFORMATION

Corresponding Author

Supriya Chakrabarti – School of Engineering, Ulster University, Belfast BT15 1AP Northern Ireland, U.K.; orcid.org/0000-0001-5175-2884; Email: s.chakrabarti@ulster.ac.uk

Authors

Abhijit Ganguly – School of Engineering, Ulster University, Belfast BT15 1AP Northern Ireland, U.K.; orcid.org/0000-0002-8852-2721

Ruairi J. McGlynn – School of Engineering, Ulster University, Belfast BT15 1AP Northern Ireland, U.K.

Adam Boies – Department of Engineering, University of Cambridge, Cambridge CB2 1PZ, U.K.

Paul Maguire – School of Engineering, Ulster University, Belfast BT15 1AP Northern Ireland, U.K.; orcid.org/0000-0002-2725-4647

Davide Mariotti – School of Engineering, Ulster University, Belfast BT15 1AP Northern Ireland, U.K.; orcid.org/0000-0003-1504-4383

Complete contact information is available at:
<https://pubs.acs.org/10.1021/acsami.3c12944>

Notes

The authors declare no competing financial interest.

ACKNOWLEDGMENTS

S.C. thanks the support of the Department for the Economy (DfE), Northern Ireland, under the US-Ireland R&D Partnership Programme, reference number: US1160. This was also funded by the Engineering and Physical Sciences Research Council (EPSRC) award n/EP/V055232/1, EP/R008841/1, EP/M015211/1. A.G. would like to thank Dilli babu Padmanaban for technical support.

REFERENCES

- (1) Crabtree, G. W.; Dresselhaus, M. S.; Buchanan, M. V. The Hydrogen Economy. *Phys. Today* **2004**, *57* (12), 39–44.
- (2) Dresselhaus, M. S.; Thomas, I. L. Alternative Energy Technologies. *Nature* **2001**, *414* (6861), 332–337.
- (3) Nocera, D. G. The Artificial Leaf. *Acc. Chem. Res.* **2012**, *45* (5), 767–776.
- (4) Li, X.; Zhao, L.; Yu, J.; Liu, X.; Zhang, X.; Liu, H.; Zhou, W. Water Splitting: From Electrode to Green Energy System. *Nano-Micro Lett.* **2020**, *12* (1), 131.
- (5) Dong, Z.-H.; Jiang, Z.; Tang, T.; Yao, Z.-C.; Xue, D.; Niu, S.; Zhang, J.; Hu, J.-S. Rational Design of Integrated Electrodes for Advancing High-Rate Alkaline Electrolytic Hydrogen Production. *J. Mater. Chem. A* **2022**, *10* (24), 12764–12787.
- (6) Shang, X.; Tang, J.-H.; Dong, B.; Sun, Y. Recent Advances of Nonprecious and Bifunctional Electrocatalysts for Overall Water Splitting. *Sustainable Energy Fuels* **2020**, *4* (7), 3211–3228.
- (7) Sun, Y.; Delucchi, M.; Ogden, J. The Impact of Widespread Deployment of Fuel Cell Vehicles on Platinum Demand and Price. *Int. J. Hydrogen Energy* **2011**, *36* (17), 11116–11127.
- (8) Roger, I.; Shipman, M. A.; Symes, M. D. Earth-Abundant Catalysts for Electrochemical and Photoelectrochemical Water Splitting. *Nat. Rev. Chem.* **2017**, *1* (1), 0003 DOI: [10.1038/s41570-016-0003](https://doi.org/10.1038/s41570-016-0003).
- (9) Yang, J.; Guo, D.; Zhao, S.; Lin, Y.; Yang, R.; Xu, D.; Shi, N.; Zhang, X.; Lu, L.; Lan, Y.-Q.; Bao, J.; Han, M. Cobalt Phosphides Nanocrystals Encapsulated by P-Doped Carbon and Married with P-Doped Graphene for Overall Water Splitting. *Small* **2019**, *15* (10), No. 1804546.
- (10) Tang, C.; Cheng, N.; Pu, Z.; Xing, W.; Sun, X. NiSe Nanowire Film Supported on Nickel Foam: An Efficient and Stable 3D Bifunctional Electrode for Full Water Splitting. *Angew. Chem., Int. Ed.* **2015**, *54* (32), 9351–9355.
- (11) Zhang, G.; Wang, P.; Lu, W.-T.; Wang, C.-Y.; Li, Y.-K.; Ding, C.; Gu, J.; Zheng, X.-S.; Cao, F.-F. Co Nanoparticles/Co, N, S Tri-Doped Graphene Templated from In-Situ-Formed Co, S Co-Doped g-C₃N₄ as an Active Bifunctional Electrocatalyst for Overall Water Splitting. *ACS Appl. Mater. Interfaces* **2017**, *9* (34), 28566–28576.
- (12) Hou, J.; Sun, Y.; Li, Z.; Zhang, B.; Cao, S.; Wu, Y.; Gao, Z.; Sun, L. Electrical Behavior and Electron Transfer Modulation of Nickel–Copper Nanoalloys Confined in Nickel–Copper Nitrides Nanowires Array Encapsulated in Nitrogen-Doped Carbon Framework as Robust Bifunctional Electrocatalyst for Overall Water Splitting. *Adv. Funct. Mater.* **2018**, *28* (37), No. 1803278.
- (13) Gong, M.; Zhou, W.; Tsai, M.-C.; Zhou, J.; Guan, M.; Lin, M.-C.; Zhang, B.; Hu, Y.; Wang, D.-Y.; Yang, J.; Pennycook, S. J.; Hwang, B.-J.; Dai, H. Nanoscale Nickel Oxide/Nickel Heterostructures for Active Hydrogen Evolution Electrocatalysis. *Nat. Commun.* **2014**, *5* (1), No. 4695.
- (14) Anjum, M. A. R.; Okyay, M. S.; Kim, M.; Lee, M. H.; Park, N.; Lee, J. S. Bifunctional Sulfur-Doped Cobalt Phosphide Electrocatalyst Outperforms All-Noble-Metal Electrocatalysts in Alkaline Electrolyzer for Overall Water Splitting. *Nano Energy* **2018**, *53*, 286–295.
- (15) Luo, J.; Im, J. H.; Mayer, M. T.; Schreier, M.; Nazeeruddin, M. K.; Park, N.-G.; Tilley, S. D.; Fan, H. J.; Grätzel, M. Water Photolysis at 12.3% Efficiency via Perovskite Photovoltaics and Earth-Abundant Catalysts. *Science* **2014**, *345* (6204), 1593–1596, DOI: [10.1126/science.1258307](https://doi.org/10.1126/science.1258307).
- (16) Wang, H.; Lee, H.-W.; Deng, Y.; Lu, Z.; Hsu, P.-C.; Liu, Y.; Lin, D.; Cui, Y. Bifunctional Non-Noble Metal Oxide Nanoparticle Electrocatalysts through Lithium-Induced Conversion for Overall Water Splitting. *Nat. Commun.* **2015**, *6* (1), No. 7261.
- (17) Shah, A. H.; Zhang, Z.; Huang, Z.; Wang, S.; Zhong, G.; Wan, C.; Alexandrova, A. N.; Huang, Y.; Duan, X. The Role of Alkali Metal Cations and Platinum-Surface Hydroxyl in the Alkaline Hydrogen Evolution Reaction. *Nat. Catal.* **2022**, *5* (10), 923–933.
- (18) Yu, X.; Ye, S. Recent Advances in Activity and Durability Enhancement of Pt/C Catalytic Cathode in PEMFC: Part II: Degradation Mechanism and Durability Enhancement of Carbon Supported Platinum Catalyst. *J. Power Sources* **2007**, *172* (1), 145–154.
- (19) Winter, M.; Brodd, R. J. What Are Batteries, Fuel Cells, and Supercapacitors? *Chem. Rev.* **2004**, *104* (10), 4245–4270.
- (20) Brunet, P.; McGlynn, R. J.; Alessi, B.; Smail, F.; Boies, A.; Maguire, P.; Mariotti, D. Surfactant-Free Synthesis of Copper Nanoparticles and Gas Phase Integration in CNT-Composite Materials. *Nanoscale Adv.* **2021**, *3* (3), 781–788.
- (21) McGlynn, R. J.; Brunet, P.; Chakrabarti, S.; Boies, A.; Maguire, P.; Mariotti, D. High Degree of N-Functionalization in Macroscopically Assembled Carbon Nanotubes. *J. Mater. Sci.* **2022**, *57* (28), 13314–13325.
- (22) Tan, W.; Stallard, J. C.; Smail, F. R.; Boies, A. M.; Fleck, N. A. The Mechanical and Electrical Properties of Direct-Spun Carbon Nanotube Mat-Epoxy Composites. *Carbon* **2019**, *150*, 489–504.
- (23) Jayasinghe, C.; Chakrabarti, S.; Schulz, M. J.; Shanov, V. Spinning Yarn from Long Carbon Nanotube Arrays. *J. Mater. Res.* **2011**, *26* (5), 645–651.
- (24) Buang, N. A.; Fadil, F.; Majid, Z. A.; Shahir, S. Characteristic of Mild Acid Functionalized Multiwalled Carbon Nanotubes towards High Dispersion with Low Structural Defects. *Dig. J. Nanomater. Biostruct.* **2012**, *7*, 33–39.
- (25) Suhr, J.; Zhang, W.; Ajayan, P. M.; Koratkar, N. A. Temperature-Activated Interfacial Friction Damping in Carbon Nanotube Polymer Composites. *Nano Lett.* **2006**, *6* (2), 219–223.
- (26) Chakrabarti, S.; Carolan, D.; Alessi, B.; Maguire, P.; Svrcek, V.; Mariotti, D. Microplasma-Synthesized Ultra-Small NiO Nanocrystals, a Ubiquitous Hole Transport Material. *Nanoscale Adv.* **2019**, *1* (12), 4915–4925.
- (27) McGlynn, R. J. *Development of Atmospheric-Pressure Plasma Processes and Systems to Tailor Nanomaterials Properties to Application Requirements*; Ulster University, 2019.
- (28) Ganguly, A.; Sharma, S.; Papakonstantinou, P.; Hamilton, J. Probing the Thermal Deoxygenation of Graphene Oxide Using High-Resolution In Situ X-Ray-Based Spectroscopies. *J. Phys. Chem. C* **2011**, *115* (34), 17009–17019.
- (29) Francisco, W.; Ferreira, E. V.; Ferreira, E. V.; Cividanes, L. D.; Coutinho, A. D.; Thim, G. P. Functionalization of Multi-Walled Carbon Nanotube and Mechanical Property of Epoxy-Based Nanocomposite. *J. Aerosp. Technol. Manag.* **2015**, *7* (3), 289–293, DOI: [10.5028/jatm.v7i3.485](https://doi.org/10.5028/jatm.v7i3.485).
- (30) Dresselhaus, M. S.; Dresselhaus, G.; Saito, R.; Jorio, A. Raman Spectroscopy of Carbon Nanotubes. *Phys. Rep.* **2005**, *409* (2), 47–99.

- (31) Saito, R.; Dresselhaus, G.; Dresselhaus, M. S. *Physical Properties of Carbon Nanotubes*; Published by Imperial College Press and distributed by World Scientific Publishing Co., 1998; p 272.
- (32) Dresselhaus, M. S.; Eklund, P. C. Phonons in Carbon Nanotubes. *Adv. Phys.* **2000**, *49* (6), 705–814.
- (33) Campos-Roldán, C. A.; Alonso-Vante, N. The Oxygen Reduction and Hydrogen Evolution Reactions on Carbon Supported Cobalt Diselenide Nanostructures. *J. Electrochem. Soc.* **2020**, *167* (2), 026507.
- (34) Kozbial, A.; Zhou, F.; Li, Z.; Liu, H.; Li, L. Are Graphitic Surfaces Hydrophobic? *Acc. Chem. Res.* **2016**, *49* (12), 2765–2773.
- (35) Dsouza, S. D.; Buerkle, M.; Brunet, P.; Maddi, C.; Padmanaban, D. B.; Morelli, A.; Payam, A. F.; Maguire, P.; Mariotti, D.; Svrcek, V. The Importance of Surface States in N-Doped Carbon Quantum Dots. *Carbon* **2021**, *183*, 1–11.
- (36) McKenna, J.; Patel, J.; Mitra, S.; Sojn, N.; Švrček, V.; Maguire, P.; Mariotti, D. Synthesis and Surface Engineering of Nanomaterials by Atmospheric-Pressure Microplasmas. *Eur. Phys. J. Appl. Phys.* **2011**, *56* (2), 24020.
- (37) Mitra, S.; Cook, S.; Švrček, V.; Blackley, R. A.; Zhou, W.; Kovač, J.; Cvelbar, U.; Mariotti, D. Improved Optoelectronic Properties of Silicon Nanocrystals/Polymer Nanocomposites by Microplasma-Induced Liquid Chemistry. *J. Phys. Chem. C* **2013**, *117* (44), 23198–23207.
- (38) Lee, M. M.; Teuscher, J.; Miyasaka, T.; Murakami, T. N.; Snaith, H. J. Efficient Hybrid Solar Cells Based on Meso-Superstructured Organometal Halide Perovskites. *Science* **2012**, *338* (6107), 643–647.
- (39) Bi, D.; Gao, P.; Scopelliti, R.; Oveisi, E.; Luo, J.; Grätzel, M.; Hagfeldt, A.; Nazeeruddin, M. K. High-Performance Perovskite Solar Cells with Enhanced Environmental Stability Based on Amphiphile-Modified $\text{CH}_3\text{NH}_3\text{PbI}_3$. *Adv. Mater.* **2016**, *28* (15), 2910–2915.
- (40) You, J.; Yang, Y.; Hong, Z.; Song, T.-B.; Meng, L.; Liu, Y.; Jiang, C.; Zhou, H.; Chang, W.-H.; Li, G.; Yang, Y. Moisture Assisted Perovskite Film Growth for High Performance Solar Cells. *Appl. Phys. Lett.* **2014**, *105* (18), No. 183902.
- (41) Li, X.; Dongqin, B.; Chenyi, Y.; Jean-David, D.; Jingshan, L.; Mohammed, Z. S.; Anders, H.; Michael, G. A Vacuum Flash-Assisted Solution Process for High-Efficiency Large-Area Perovskite Solar Cells. *Science* **2016**, *353* (6294), 58–62.
- (42) Yin, J.; Cao, J.; He, X.; Yuan, S.; Sun, S.; Li, J.; Zheng, N.; Lin, L. Improved Stability of Perovskite Solar Cells in Ambient Air by Controlling the Mesoporous Layer. *J. Mater. Chem. A* **2015**, *3* (32), 16860–16866.
- (43) Liu, D.; Lu, Q.; Luo, Y.; Sun, X.; Asiri, A. M. NiCo_2S_4 Nanowires Array as an Efficient Bifunctional Electrocatalyst for Full Water Splitting with Superior Activity. *Nanoscale* **2015**, *7* (37), 15122–15126.
- (44) Zheng, X.; Han, X.; Liu, H.; Chen, J.; Fu, D.; Wang, J.; Zhong, C.; Deng, Y.; Hu, W. Controllable Synthesis of Ni_xSe ($0.5 \leq x \leq 1$) Nanocrystals for Efficient Rechargeable Zinc–Air Batteries and Water Splitting. *ACS Appl. Mater. Interfaces* **2018**, *10* (16), 13675–13684.
- (45) Ledendecker, M.; Krick Calderón, S.; Papp, C.; Steinrück, H.-P.; Antonietti, M.; Shalom, M. The Synthesis of Nanostructured Ni_3P_4 Films and Their Use as a Non-Noble Bifunctional Electrocatalyst for Full Water Splitting. *Angew. Chem., Int. Ed.* **2015**, *54* (42), 12361–12365.
- (46) Du, S.; Ren, Z.; Zhang, J.; Wu, J.; Xi, W.; Zhu, J.; Fu, H. Co_3O_4 Nanocrystal Ink Printed on Carbon Fiber Paper as a Large-Area Electrode for Electrochemical Water Splitting. *Chem. Commun.* **2015**, *51* (38), 8066–8069.
- (47) Chen, G.-F.; Ma, T. Y.; Liu, Z.-Q.; Li, N.; Su, Y.-Z.; Davey, K.; Qiao, S.-Z. Efficient and Stable Bifunctional Electrocatalysts $\text{Ni}/\text{Ni}_x\text{M}_y$ ($\text{M} = \text{P}, \text{S}$) for Overall Water Splitting. *Adv. Funct. Mater.* **2016**, *26* (19), 3314–3323.
- (48) McCrory, C. C. L.; Jung, S.; Peters, J. C.; Jaramillo, T. F. Benchmarking Heterogeneous Electrocatalysts for the Oxygen Evolution Reaction. *J. Am. Chem. Soc.* **2013**, *135* (45), 16977–16987.
- (49) Bard, A. J.; Faulkner, L. R. *Electrochemical Methods: Fundamentals and Applications*, 2nd ed.; John Wiley and Sons, 2001.
- (50) Lai, B.; Singh, S. C.; Bindra, J. K.; Saraj, C. S.; Shukla, A.; Yadav, T. P.; Wu, W.; McGill, S. A.; Dalal, N. S.; Srivastava, A.; Guo, C. Hydrogen Evolution Reaction from Bare and Surface-Functionalized Few-Layered MoS_2 Nanosheets in Acidic and Alkaline Electrolytes. *Mater. Today Chem.* **2019**, *14*, No. 100207.
- (51) Strmcnik, D.; Uchimura, M.; Wang, C.; Subbaraman, R.; Danilovic, N.; van der Vliet, D.; Paulikas, A. P.; Stamenkovic, V. R.; Markovic, N. M. Improving the Hydrogen Oxidation Reaction Rate by Promotion of Hydroxyl Adsorption. *Nat. Chem.* **2013**, *5* (4), 300–306.
- (52) Gu, Y.; Chen, S.; Ren, J.; Jia, Y. A.; Chen, C.; Komarneni, S.; Yang, D.; Yao, X. Electronic Structure Tuning in $\text{Ni}_3\text{FeN}/\text{r-GO}$ Aerogel toward Bifunctional Electrocatalyst for Overall Water Splitting. *ACS Nano* **2018**, *12* (1), 245–253.
- (53) Danilovic, N.; Subbaraman, R.; Strmcnik, D.; Chang, K.-C.; Paulikas, A. P.; Stamenkovic, V. R.; Markovic, N. M. Enhancing the Alkaline Hydrogen Evolution Reaction Activity through the Bifunctionality of $\text{Ni}(\text{OH})_2/\text{Metal}$ Catalysts. *Angew. Chem., Int. Ed.* **2012**, *51* (50), 12495–12498.
- (54) Shinagawa, T.; Garcia-Esparza, A. T.; Takanahe, K. Insight on Tafel Slopes from a Microkinetic Analysis of Aqueous Electrocatalysis for Energy Conversion. *Sci. Rep.* **2015**, *5* (1), No. 13801.
- (55) Ji, L.; Wang, J.; Teng, X.; Meyer, T. J.; Chen, Z. CoP Nanoframes as Bifunctional Electrocatalysts for Efficient Overall Water Splitting. *ACS Catal.* **2020**, *10* (1), 412–419.
- (56) Duan, W.; Han, S.; Fang, Z.; Xiao, Z.; Lin, S. In Situ Filling of the Oxygen Vacancies with Dual Heteroatoms in Co_3O_4 for Efficient Overall Water Splitting. *Molecules* **2023**, *28*, 4134.
- (57) Jiao, L.; Zhou, Y.-X.; Jiang, H.-L. Metal–Organic Framework-Based CoP/Reduced Graphene Oxide: High-Performance Bifunctional Electrocatalyst for Overall Water Splitting. *Chem. Sci.* **2016**, *7* (3), 1690–1695.
- (58) Zhang, Q.; Zhang, C.; Liang, J.; Yin, P.; Tian, Y. Orthorhombic α - NiOOH Nanosheet Arrays: Phase Conversion and Efficient Bifunctional Electrocatalysts for Full Water Splitting. *ACS Sustainable Chem. Eng.* **2017**, *5* (5), 3808–3818.
- (59) Veeramani, K.; Shanmugapriya, S.; Young Kim, J.; Surendran, S.; Jun Moon, D.; Janani, G.; Cyril Jesudass, S.; Mahadik, S.; Choi, H.; Jung, P.; Goo Kim, I.; Heo, J.; Hong, K.; Kim, T.-H.; Il Park, Y.; Sim, U. Synergistically Enhanced Electrocatalytic Performance of NiO Infused Crystalline Graphitic Carbon towards Overall Water Splitting. *Mater. Lett.* **2024**, *356*, No. 135593.
- (60) Hoang, V. C.; Dinh, K. N.; Gomes, V. G. Hybrid Ni/NiO Composite with N-Doped Activated Carbon from Waste Cauliflower Leaves: A Sustainable Bifunctional Electrocatalyst for Efficient Water Splitting. *Carbon* **2020**, *157*, 515–524.
- (61) Ghosh, S.; Kadam, S. R.; Kolatkar, S.; Neyman, A.; Singh, C.; Enyashin, A. N.; Bar-Ziv, R.; Bar-Sadan, M. W Doping in Ni_{12}P_5 as a Platform to Enhance Overall Electrochemical Water Splitting. *ACS Appl. Mater. Interfaces* **2022**, *14* (1), 581–589.
- (62) Wang, B.; Liu, Q.; Yuan, A.; Shi, Q.; Jiang, L.; Yang, W.; Yang, T.; Hou, X. A Facile and Green Strategy for Mass Production of Dispersive FeCo-Rich Phosphides@N,P-Doped Carbon Electrocatalysts toward Efficient and Stable Rechargeable Zn–Air Battery and Water Splitting. *J. Mater. Sci. Technol.* **2024**, *182*, 1–11.
- (63) Wang, D.; Zhang, C.; Hu, J.; Zhuang, T.; Lv, Z. Nitriding-Reduction Fabrication of Coraloid $\text{CoN}/\text{Ni}/\text{NiO}$ for Efficient Electrocatalytic Overall Water Splitting. *J. Colloid Interface Sci.* **2024**, *655*, 217–225.
- (64) Walendzik, I.; Kordek-Khalil, K.; Rutkowski, P. Quick-to-Synthesize Hybrid Electrodes Composed of Activated Carbon Cloth with Co/Fe-Based Films as Bifunctional Electrocatalysts for Water Splitting. *Int. J. Hydrogen Energy* **2023**, *48* (66), 25741–25754.
- (65) You, B.; Jiang, N.; Sheng, M.; Bhushan, M. W.; Sun, Y. Hierarchically Porous Urchin-Like Ni_2P Superstructures Supported on Nickel Foam as Efficient Bifunctional Electrocatalysts for Overall Water Splitting. *ACS Catal.* **2016**, *6* (2), 714–721.
- (66) Li, J.; Yan, M.; Zhou, X.; Huang, Z.-Q.; Xia, Z.; Chang, C.-R.; Ma, Y.; Qu, Y. Mechanistic Insights on Ternary $\text{Ni}_{2-x}\text{Co}_x\text{P}$ for Hydrogen Evolution and Their Hybrids with Graphene as Highly Efficient and Robust Catalysts for Overall Water Splitting. *Adv. Funct. Mater.* **2016**, *26* (37), 6785–6796.